

Multifunctional reactive MALDI matrix enabling high-lateral resolution dual polarity MSI and lipid C=C position-resolved MS²I

Fabian Wäldchen¹, Franziska Mohr², Andreas H. Wagner² and Sven Heiles^{1*}

¹Institute of Inorganic and Analytical Chemistry, Analytical Chemistry, Justus Liebig University Giessen, Heinrich Buff Ring 17, 35392 Giessen, Germany

²Department of Cardiovascular Physiology, Heidelberg University, Im Neuenheimer Feld 326, 69120 Heidelberg, Germany

ABSTRACT: Local lipid variations in tissues are readily revealed with mass spectrometry imaging (MSI) methods and resulting lipid distributions serve as bioanalytical signatures to reveal cell- or tissue-specific lipids. Comprehensive MSI lipid mapping requires measurements in both ion polarities. Additionally, structural lipid characterization is necessary to link lipid structure to lipid function. Whereas some structural elements of lipids are readily derived from high-resolution mass spectrometry (MS) and tandem-MS (MSⁿ), the localization of C=C double bonds (DBs) requires specialized fragmentation and/or functionalization methods. In this work, we identify a multifunctional matrix-assisted laser desorption/ionization (MALDI) matrix for spatially-resolved lipidomics investigations that reacts with lipids in Paternò-Büchi (PB) reactions during laser irradiation facilitating DB position assignment and allows dual polarity high-resolution MALDI-MSI and MALDI MS²I studies. By screening twelve compounds for improved ionization efficiency in positive/negative ion mode and PB functionalization yield compared to the previously introduced reactive MALDI matrix benzophenone, benzoylpyridine (BzPy) is identified as the best candidate. The multifunctional character of the new matrix enables DB localization of authentic standards belonging to twelve lipid classes and helps to assign 506/365 lipid features in positive/negative ion mode from mouse cerebellum tissue. The analytical capabilities of BzPy as a multifunctional MALDI-MSI matrix are demonstrated by imaging endogenous and PB-functionalized lipids in mouse kidney sections with 7 μm lateral resolution in both ion modes. Tracking diagnostic lipid DB position fragment ions in mouse pancreas tissue with down to 10 μm pixel size allows to identify islets of Langerhans associated lipid isomer upregulation or depletion.

INTRODUCTION

In-depth lipid characterization of cells, tissues, or body fluids is at the heart of lipidomics that promises novel insights into lipid biology and aims to use lipid biomarkers or lipid signatures as diagnostic probes to monitor disease progression.^{1,2} Lipid analysis requires comprehensive charting of expressed lipids but also a detailed characterization of lipid distributions and structures.³ This is because disease-associated lipid abundance alterations or implications of subtle structural changes are often unpredictable as most of the intertwined enzymatic processes involved in lipid metabolism are yet to be unraveled.⁴⁻⁶ For example, the unfolded protein response (UPR) of eukaryotic cells increases when the level of saturated lipids in the cell membrane of the endoplasmic reticulum increases. This suggests that the UPR regulatory machinery can sense cell membrane composition offering a potential connecting to reports about endoplasmic reticulum stress induced by obesity, high-fat diets, or type 2 diabetes.^{7,8} The mechanism of lipid composition sensing, however, remains unclear. This demonstrates that many details of lipid metabolism in the context of biology and medicine will benefit from bioanalytical methods that can provide a comprehensive picture of lipid composition and distribution but also investigate lipid structure variations to reveal unexpected effects in lipid biology.

One of the most widely used untargeted bioanalytic tools in lipidomics is mass spectrometry (MS).² This is because direct infusion measurements, often using electrospray ionization

(ESI),⁹ desorption-electrospray ionization¹⁰ and matrix-assisted laser desorption/ionization (MALDI)¹¹, allow to distinguish a multitude of lipids by accurate mass-to-charge, m/z , values and assign their sum formulae when employing state-of-the-art mass spectrometers. Tandem MS (MSⁿ), first and foremost collision-induced dissociation (CID), reveal lipid fatty acid composition and lipid class.¹² Hyphenated techniques such as liquid chromatography (LC) or ion-mobility spectrometry (IMS) can further improve the performance of MS-based lipidomics by separating isobaric and isomeric lipid compounds.¹³ However, the assignment of mass spectrometric features to specific lipid structures, especially for glycerolipids, glycerophospholipids, sphingolipids, and glycolipids, remains challenging. Therefore, recent years have seen a surge in novel tandem MS methods that allow to distinguish structural features of isomeric lipids. Especially for C=C (DB) position assignment, many novel mass spectrometric tools, like e.g. ultraviolet (UV) photodissociation mass spectrometry,¹⁴⁻¹⁷ radical-directed dissociation,^{18,19} ozone-induced dissociation (OzID),²⁰ infrared (IR) action spectroscopy of ultra-cold ions,²¹ have been reported. In-solution functionalization via epoxidation^{22,23} or photochemical Paternò-Büchi (PB) functionalization prior ESI is also capable to identify lipid DB positions.²⁴⁻²⁸ The latter functionalization scheme, pioneered by Ma and Xia,²⁹ has been used by numerous groups to assign DB positions in direct infusion and LC-MS workflows.^{30,31} Lipid DB isomer assignment from surfaces or local alterations of lipid isomer abundances in tissue, however,

require desorption-based ionization methods.^{14,23,20,32} For example, MALDI MS and MS imaging (MSI) tools were developed that enable pinpointing lipid DB positions. MALDI-MSI and OzID were combined by Paine *et al.* to visualize DB position isomer distributions in rat brain sections with down to 80 μm lateral resolution.²⁰ Bednařik *et al.* developed on-tissue PB and ozonolysis functionalization methods for lipids to track DB position variations in brain and colon tissue with MALDI-MS²I and MALDI-MS²I with down to 25 μm and 15 μm , respectively.^{33,34} In one of our recent studies we identified benzophenone (BPh) as compound that can act as MALDI matrix and reacts with lipids in a PB reaction during laser irradiation, a process termed PB reactive MALDI.³⁵ This enabled *in situ* derivatization, DB assignment and imaging of lipids in mouse brain sections and parasites with a pixel size down to 15 μm . These studies have revealed that some DB position isomers are associated with distinct histological features and that lipid isomer abundances can change upon disease progression. As the biochemical origin of these organizational preferences is unknown, charting of spatially-resolved lipid DB position maps are required to develop a refined picture of local lipid metabolism.³⁶ In order to develop a comprehensive map of lipid abundances and DB position expression in tissue, MALDI methods are required that facilitate high lateral resolution measurements (below 20 μm), allow DB position assignment and cover a broad range of lipid classes. Aside from appropriate MALDI equipment, the MALDI matrix is particularly important.^{37,38} The matrix needs to enable high lateral resolution measurements, allow or facilitate DB position assignment and enable dual-polarity measurements to cover a broad range of the chemically diverse class of lipids. MALDI matrices typically used for high-resolution MSI measurements, such as 2,5-dihydroxybenzoic acid (DHB)³⁹ or 9-aminoacridine (9-AA)⁴⁰, yield best results in positive or negative ion mode. Novel tailor-made matrices, like acid/base bifunctional MALDI matrices, improve the detection of positive/negative ions.⁴¹ MALDI matrices for low molecular weight compounds were recently reviewed.⁴² However, simultaneous detection of lipids in both ion modes, DB position assignment and high-resolution MALDI-MSI has not been achieved yet.

Here we evaluated the ability of twelve BPh-derivatives to serve as PB reactive MALDI matrix and improve lipid coverage, DB position assignment as well as the lateral resolution in MALDI-MSI and MALDI-MS²I compared to BPh. The reactive PB matrix with the best-combined performance characteristics in terms of ion signal intensity and DB diagnostic fragment ion intensities is demonstrated to allow dual polarity MALDI-MSI with down to 7 μm lateral resolution, increases the lipid class coverage compared to BPh results, facilitates DB position assignment of 12 lipid classes in positive or negative ion mode, and enables DB position-resolved MALDI-MS²I with down to 10 μm pixel size. The capabilities of this novel PB reactive matrix are showcased by imaging histological features of mouse kidney/pancreas tissue. In particular, glomeruli in the kidney are imaged in both ion polarities in MALDI-MSI experiments, and DB position resolved MALDI-MS²I results of Langerhans-islet of the murine pancreas are presented.

EXPERIMENTAL SECTION

Materials and Lipid Nomenclature. Lipid standards and lipid extracts were purchased from Avanti Polar Lipids (Ala-

bama, USA) and NOF Corporation (New York, USA). Benzophenone (BPh), 2-benzoylpyridine (BzPy), di(pyridine-2-yl)methanone (D2PyM), di(pyridine-3-yl)methanone (D3PyM), 4-benzoylbenzoic acid (4-BzBA), 4,4'-difluorobenzophenone (DFBPh), 2-aminobenzophenone (2-ABPh), 3-aminobenzophenone (3-ABPh), 4-aminobenzophenone (4-ABPh), 1-isoquinolinyl phenyl ketone (IQPK), diazafluorenone (DAF), 9-fluorenone (9F), 2,2',4,4' tetrahydroxybenzophenone (THBPh) (Figure S1) used in screening experiments were purchased from Sigma-Aldrich. All chemicals (analytical purity) used without further purification. The lipid nomenclature introduced by Liebisch *et al.*⁴³ is adapted in this manuscript except for the DB position notation for which the *n*-nomenclature is employed, where a DB at position *x* counted from the aliphatic end of the hydrocarbon residue (ω -carbon) is noted as "*n-x*". Consequently, a ω -6 fatty acid with 18 C-atoms and one DB is abbreviated by FA 18:1 (*n*-6).

Tissue and sample preparation. Cryotome (HM525, Thermo Scientific, Dreieich, Germany) sectioning of the mouse brain (C57BL6/N male and female mice 12–20 weeks of age), mouse kidney (wt/wt male mouse 39 weeks of age) and mouse pancreas (wt/wt female mouse 12 weeks of age) samples was done at $-20\text{ }^{\circ}\text{C}$ and the resulting tissue sections (20 μm thickness) were thaw-mounted on glass slides. Organ samples and tissue sections were stored at $-80\text{ }^{\circ}\text{C}$ until further use. All animal experiments were performed with the permission of the Regional Council Karlsruhe (permission number G-53/17) and conformed to the Guide for the Care and Use of Laboratory Animals (NIH Publication No. 85-23, revised 2011). The mice were housed in the Interfaculty Biomedical Research Facility (IBF) of Heidelberg University, Germany. Matrices were applied by sublimation/resublimation onto tissue sections using a homebuilt setup (Figure S2 left).⁴⁴ Lipid standards and lipid extracts were spotted onto glass slides by dried-droplet deposition (1 μL volume) of 10^{-3} M solutions in methanol, chloroform or dichloromethane. After lipid deposition, 10^{-2} M solutions of the respective matrix was spotted onto the lipid sample by dried-droplet deposition (1 μL droplet volume).

MALDI-MSI. An AP-SMALDI5-AF MSI ion source (TransMIT GmbH, Giessen, Germany) coupled to an orbital trapping mass spectrometer (Q Exactive or Q Exactive HF, Thermo Fisher Scientific GmbH, Bremen, Germany) was employed for the MALDI-MS, -MS², -MS² and -MS²I experiments. The full-pixel mode was used for MALDI-MS, -MS² and -MS²I experiments with 10 – 20 μm pixel size. In full-pixel mode, the ablation area per sampled surface region is increased by quickly moving the sample while operating the ablation laser with a high repetition rate.³⁵ For MALDI-MSI measurements a laser size of 7 μm was used to locally probe the sample surface without steering the laser across the sample. For MS-, MSI-, MS²- and MS²I the following settings were used: mass resolution at *m/z* 200: 140,000 (Q Exactive) or 240,000 (Q Exactive HF), higher-energy collisional dissociation (HCD) normalized collision energy setting: between 18 and 44, inlet capillary temperature: 250 $^{\circ}\text{C}$, S-lens setting: 100. External mass calibration for MALDI-MSI was performed using the ion signals of protonated PC 34:1 and deprotonated PI 38:4 in positive and negative ion mode, respectively.

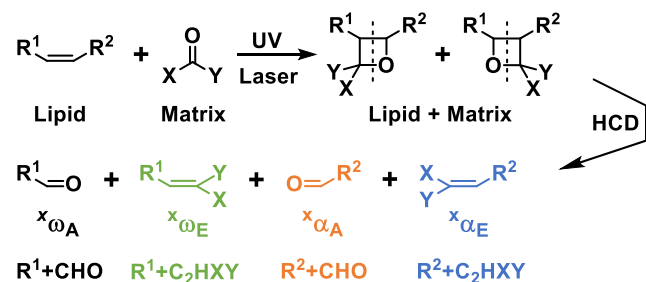
Microscopy and UV/Vis spectroscopy. Immunofluorescence staining of mouse kidney and mouse pancreas tissue sections was done following the Supporting Protocol 1 and Supporting Protocol 2, respectively. Optical microscope images

and fluorescence microscope images were acquired by the aid of a Keyence VHX-5000 digital microscope (Keyence Deutschland GmbH, Neu-Isenburg, Germany) and an Axiovert 2000M microscope (Zeiss, Oberkochen, Germany), respectively. UV/Vis measurements of matrix-covered cuvettes were performed with a V-550 (JASCO GmbH, Pfungstadt, Germany) instrument.

Data analysis and visualization. The Thermo XCalibur Qual Browser was used for manual analysis of individual or averaged mass spectra, whereas MS images were processed with the Mirion imaging software.⁴⁵ All images were created with a histogram bin width of 0.01 u and an absolute m/z variance of 0.01 u. Ion-signal intensities used for MALDI-MSI and -MS²I were normalized to the total ion current (TIC) per pixel and the highest signal intensity per image. For lipid assignment in MALDI-MSI experiments, accurate m/z values were compared to exact m/z values using data bank searches in LIPID MAPS. The data bank was searched for protonated, sodiated, potassiumated, and deprotonated ions in the positive and negative ion mode, respectively. Annotations were included in a putative lipid list if their relative m/z deviation was below ± 10 ppm. The list was not validated by MS² experiments. In case of multiple hits for one m/z value, only the annotation with the lowest mass deviation is listed. The pseudo-PB or apparent PB reaction yield, Y , was calculated by using MS intensities of one particular ion type ($[M+H]^+$, $[M+Na]^+$, $[M+K]^+$ or $[M-H]^-$) according to the formula $Y = (\text{product ion intensity}) / (\text{product ion intensity} + \text{unfunctionalized lipid precursor ion intensity}) \cdot 100\%$.

Fragment ion nomenclature. Upon dissociative cleavage of intact oxetanes formed in PB reactions, four fragment ions per DB position can result from HCD (Scheme 1). Fragment ions will be labeled according to the nomenclature introduced in Scheme 1. Fragment ions that contain the lipid head group will be labeled as α -ions. Complementary fragment ions that only consist of the remaining FA residue are classified as ω -ions. The location, x , of the dissociated DB, according to the above introduced DB nomenclature, is added as superscript. The subscript A or E indicates if the fragment ions formally contain an aldehyde or not, respectively.

Scheme 1. Paternò-Büchi functionalization and higher-collisional energy dissociation of functionalized lipids.



R^2 corresponds to the lipid residue containing the lipid head group, whereas R^1 comprises the remaining hydrocarbon chain.

RESULTS AND DISCUSSION

Screening of PB reactive matrices. To improve the performance of our PB reactive MALDI scheme in terms of MS intensities and PB reaction yields compared to BPh results, mixtures of twelve BPh derivatives with PC 18:1($n-9$)/18:1($n-9$) were investigated by MALDI-MS as well as -MS² and results

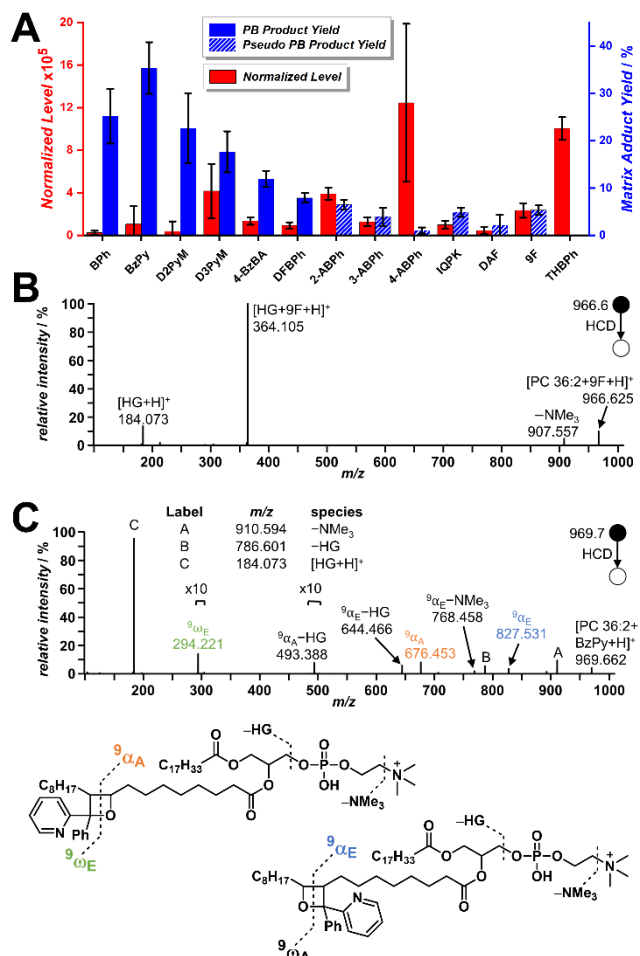


Figure 1. (A) Normalized level (red bars) and matrix adduct formation yield (blue bars) of screened matrices. PB product and pseudo-PB product ions are highlighted by full blue bars and shaded blue bars, respectively. Error bars represent one standard deviation. Positive ion mode MALDI-MS²-spectra of (B) [PC 18:1($n-9$)/18:1($n-9$)+9F+H]⁺ and (C) [PC 18:1($n-9$)/18:1($n-9$)+BzPy+H]⁺ and retro-PB cleavage sites are indicated. NL – normalized level; HG – head group; NMe₃ – trimethylamine.

are shown in Figure 1 and S3. All tested matrices contain a carbonyl group to ensure PB reactivity and aromatic residues for UV absorption (Figure S1, S4). Additional hydroxy-, carboxy- and amine groups are attached to the aromatic residues of THBPh, 4-BzBA and 2-/3-/4-ABPh to promote the protonation or deprotonation of analytes, respectively. Other potential matrices contain fluorine substituents (DFBPh), covalently interlinked aromatic residues (DAF, 9F), an expanded aromatic system (IQPK) or pyridine instead of benzene moieties (BzPy, D2PyM, D3PyM). A comparison of the normalized level (NL) of protonated PC 18:1($n-9$)/18:1($n-9$) as a relative measure for ionization efficiency and the apparent PB reaction yield derived from the [PC 18:1($n-9$)/18:1($n-9$)+matrix+H]⁺ signal for all studied matrix compounds and BPh is shown in Figure 1A. Every tested compound performed as MALDI matrix affording NL values ranging from 3.79·10⁴ for D2PyM to 1.24·10⁶ for 4-ABPh which is a 1.5- and 49.6-fold NL improvement compared to BPh, respectively. In contrast, most apparent PB reaction yields of the [PC 18:1($n-9$)/18:1($n-9$)+matrix+H]⁺ signal were

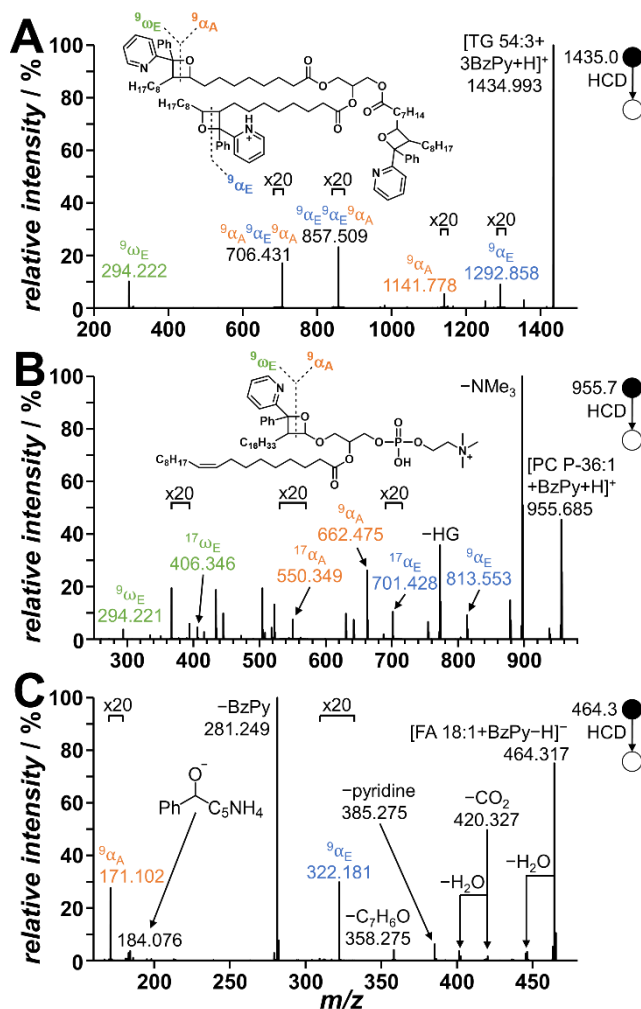


Figure 2. MALDI-MS² spectra of BzPy-functionalized (A) TG 18:1(*n*-9)/18:1(*n*-9)/18:1(*n*-9), (B) PC P-18:0/18:1(*n*-9) and (C) FA 18:1(*n*-9) are shown. See Figure S7 for additional ion assignments.

lower or comparable to BPh results. In particular, only the matrices BzPy, D2PyM and D3PyM give apparent PB yields of 35±6%, 23±7%, and 18±4%, respectively, that are higher or comparable to the 25±6% obtained for BPh.

In the next set of experiments, MALDI-MS² of [PC 18:1(*n*-9)/18:1(*n*-9)+matrix+H]⁺ ions was performed to distinguish non-selective lipid-matrix compounds from PB reaction products. As highlighted in Scheme 1, collisional activation of PB product ions results in a set of product ion pairs per DB upon retro-PB oxetane cleavage, whereas only dissociation of ions/molecules containing intact matrix molecules is expected in the absence of PB reactivity. Two representative MALDI-MS² spectra that indicate the absence of PB reactivity and are characteristic for PB reactive matrices are shown in Figure 1B and 1C, respectively. Whereas experiments with 9F resulted in the formation of [PC 18:1(*n*-9)/18:1(*n*-9)+9F+H]⁺ ions with an apparent reaction yield of 5±1% (Figure S3A), no retro-PB ions are present in the MALDI-MS² spectrum (Figure 1B). This indicates that 9F is not PB reactive. Consequently, pseudo-PB reaction yields are labeled in Figure 1A (shaded blue). This is in contrast to fragment ions in MALDI-MS² spectra of [PC 18:1(*n*-9)/18:1(*n*-9)+BzPy+H]⁺ (Figure 1C). The ions at *m/z* 676.453 and *m/z* 827.531 are in line with retro-PB cleavage

of oxetanes resulting in ⁹α_A and ⁹α_E fragments (Scheme 1) consistent with a PB reaction between BzPy and PC 18:1(*n*-9)/18:1(*n*-9) during MALDI. Additionally, the signal at *m/z* 294.221 indicates the protonation of the pyridine moiety affording ⁹ω_E fragments not observed with BPh (Figure S5). According to the MALDI-MS² results not only BzPy but also D2PyM, D3PyM, 4-BzBA, and DFBPh are PB reactive MALDI matrices as highlighted in Figure 1A.

These results suggest that PB reactivity is diminished if hydroxy- or amino-groups are present or conformational flexibility of matrix moieties is decreased as a result of covalent interlinking of aromatic residues. The reactivity trend of identified PB reactive matrices, however, does not correlate with available photochemical reactivity descriptors such as matrix extinction coefficients at 343 nm or phosphorescence quantum yields. Out of all tested matrices, only BzPy, D2PyM and D3PyM afforded PB product ions with reaction yields higher or comparable to BPh. MALDI-MS² of these compounds provide α and ω retro-PB fragment ions (Figure 1C, S6). Because the PB reaction yield and NL values for α ions are higher for BzPy than for BPh, D2PyM and D3PyM, BzPy was used throughout the rest of the manuscript as reactive MALDI matrix.

PB product yields and DB assignment of lipids in positive and negative ion mode. To evaluate the number of lipid classes with addressable DBs compared to BPh and other DB localization methods, the DB functionalization scope of the BzPy was investigated. Table S1 summarizes corresponding positive and negative ion mode MALDI-MS and -MS² results. In particular, PB yields of investigated lipids (FA, SHexCer, PA, PE, PI, SM, PG, PS, HexCer, CL TG and plasmalogen PC) along with the DB positions inferred from accurate *m/z* values (mass error ≤ ±5 ppm) of fragment ions are listed. In both ion modes PB functionalized lipids will differ by 183.068 Da from unfunctionalized compounds. The α/ω fragment ion pairs corresponding to the same DB are separated by 151.079 Da (Scheme 1). Lipids and corresponding PB products are detected as [M+H]⁺ and/or [M+Na]⁺ and [M-H]⁻ ions. The apparent PB reactivity of BzPy depends on the lipid class and ion identity. In particular, the *Y* values range from 5.0% for oleic acid to 100% for TG 54:3. PB reaction yields also depend on the charge carrier identity as observed for different TG adducts. For example, PB-functionalized TG signals ([TG 54:3+BzPy+H]⁺, [TG 54:3+2BzPy+H]⁺, [TG 54:3+3BzPy+H]⁺) are higher in intensity than corresponding sodiated ion signals, even though the NL value for [TG 54:3+Na]⁺ is higher than [TG 54:3+H]⁺. As a consequence, the apparent PB yield for the sodiated PB product with the highest MS intensity is 70.8%, whereas *Y* calculated for the corresponding protonated signal is 100%. Similarly, the protonated to sodiated ion signal ratios of PB products of PI, PA, PE, and PS are increased by a factor of 2 – 600 compared to unfunctionalized species. Protonated signals of PG, CL, and TG lipids are exclusively observed for BzPy-modified compounds. These results suggest that attachment of BzPy during PB reactions can affect ionization yields of products compared to precursor ions. This is also in line with recent PB-ESI-MS results by Ma,²⁶ Xia,³¹ and our group²⁸ that documented the ability to enhance ionization efficiencies using various pyridine-containing PB-reactive compounds. Therefore, *Y* values are affected by the intrinsic PB reactivity but also by ionization efficiency changes. In general, these results indicate that BzPy

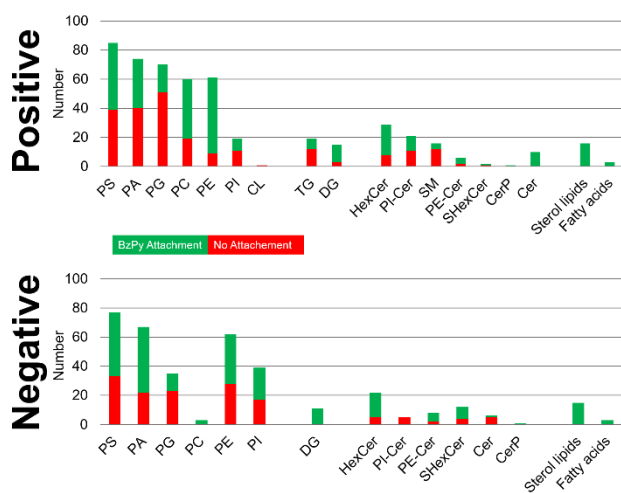


Figure 3. Number of assigned lipids and lipid classes in positive and negative ion mode from MALDI-MSI measurements of BzPy-covered mouse cerebellum tissue. Number of lipids (green) with and (red) without BzPy-attachment in the (upper row) positive and (lower row) negative ion mode. can

ionize all tested lipid standards in positive and/or negative ion mode and can increase the MS intensity of PB product ions by facilitating protonation or sodiation.

Next, HCD fragmentation of PB product ions was used to investigate the influence of lipid class and ion mode on the ability to assign DB positions. As listed in Table S1, α_A and α_E were detected for all lipid species except for PS 16:0/18:1(*n*-9) and SHexCer 42:2(*n*-9) for which the α_E signals were absent in the MS²-spectra. To the best of our knowledge, the list includes MALDI-MS² DB localization for lipids not reported before. Some representative examples are shown in Figure 2 and MS²-spectra of the other tested lipids are shown in Figure S8. For example, TG 54:3 readily reacts with BzPy during MALDI to form mono-, di- and tri- PB-functionalized protonated or sodiated ions (Figure S9). The MS² spectra of [TG 54:3+3BzPy+H]⁺ and mono-, di-functionalized protonated, and sodiated TG 54:3 are shown in Figure 2A and S9B – S9E, respectively. Similar to mono- and di-functionalized counterparts, HCD of [TG 54:3+3BzPy+H]⁺ yields α_A , α_E and ω_E fragment ions resulting from a combination of multiple retro-PB events. All HCD results for TGs exhibit protonated or sodiated ${}^9\omega_E$ ion signals. This indicates that charge carriers can migrate to or are located at BzPy. Because the appearance of ω_E ion signals documents the propensity of BzPy towards charge carriers, these results also support the finding that the ionization efficiency is changed due to BzPy attachment.

Another example for DB assignment is shown in Figure 2B for the plasmalogen PC P-18:0/18:1(*n*-9) that possess a vinylic and an isolated DB at position *n*-17 and *n*-9, respectively. HCD of [PC P-18:0/18:1(*n*-9)+BzPy+H]⁺ affords multiple DB fragment ions including protonated α_A , α_E and ω_E ions that enable DB assignment of the free and the vinylic DB. In contrast to Lin et al. who observed a preference for α_E fragments from plasmalogen DBs, α fragments were detected with similar abundances ($\alpha_E:\alpha_A = 1.4:1$).⁴⁶ To demonstrate the use of BzPy in negative ion mode DB localization, MALDI-MS² of deprotonated FA 18:1(*n*-9) (Figure 2C) and SHexCer 42:2(*n*-9) (Figure S8A) were performed. Despite the low intensity of retro-PB fragment ions (0.3% – 2.2% relative to the precursor ions), ${}^9\alpha_A/{}^9\alpha_E$ and

${}^9\alpha_A$ ions enabled DB position assignment for FA 18:1(*n*-9) and SHexCer 42:2(*n*-9) in negative ion mode using MALDI-MS² for the first time, respectively. Next, we investigated if reactive MALDI using BzPy allows us to relatively quantify DB position isomers. Solutions of the isomeric lipid standards PC 18:1(*n*-12)/18:1(*n*-12) and PC 18:1(*n*-9)/18:1(*n*-9) were mixed in defined molar ratios and MALDI-MS² experiments were performed. The MS² intensity ratios of the isomer-specific ${}^{12}\alpha_A$ and ${}^9\alpha_A$ ions linearly correlate with the molar ratios ($R^2=0.999$) showcasing the ability to differentiate and relatively quantify lipid DB position isomers using the reactive matrix BzPy (Figure S7D).

These results demonstrate the multifunctional character of BzPy as MALDI matrix: The compound enables lipid ionization in positive and negative ion mode, enhance MS signals for some lipids upon PB reaction and improves the ability introduced with BPh to identify and relatively quantify DB positions of phospholipids in positive ion mode while extending the DB addressable lipid class range.

MSI lipid class coverage in the mouse cerebellum. As the ionization of many lipid classes suffers from a known suppression effect,⁴⁷ the coverage of lipid classes in mouse cerebellum tissue was evaluated to assess the suitability of BzPy for comprehensive lipid coverage in MSI studies. In total, 508/365 lipids were annotated in the positive/negative ion mode, respectively. Figure S11A gives an overview of the numbers of assigned species in the lipid categories. Corresponding subclasses are shown in Figure S11B – S11D. Table S2 – S6 lists all assigned lipids. As expected, the assigned species are dominated by 371/283 GPLs but also 34/11 GLs, 85/54 SLs, 15/14 STs, and 3/3 FAs are present in positive/negative ion mode (Figure S11A top rows). Besides the detected unfunctionalized species (Figure S11A middle rows), the total numbers of compounds exclusively detected as BzPy adducts in the positive/negative ion mode are (Figure S11A bottom rows) GPLs (89/58), GLs (13/11), SLs (29/13), STs (15/14) and fatty acids (3/3). This underlines the advantage of using a reactive matrix that facilitates ionization. Because BzPy-attachment was observed for unsaturated and saturated lipids, BzPy most likely also reacts with the head group, in a reaction other than PB functionalization or attaches to lipids in a non-covalent manner. This is also consistent with reports by Xia³¹ and Hayen³⁰ about PB reaction by-products in in-solution reactions. The number of lipids with or without BzPy-attachment are compared in Figure 3. Using BzPy, TGs, a lipid class notoriously difficult to detect in cerebellum tissue with MALDI, were detected as BzPy adducts in the positive ion mode.^{35,11,48} The same is true for DGs but these have also been assigned as BzPy adducts in the negative ion mode. SLs and FAs exclusively appeared as BzPy-adduct signals in spectra of both polarities. This emphasizes the expanded lipid class coverage that BzPy provides in comparison to BPh.

Dual polarity high-resolution MALDI-MSI of kidney. After evaluating the matrix crystal size, PB and retro-PB reactivity, and the lipid class coverage of BzPy, the ability to perform MALDI-MSI experiments in both ion modes with pixel resolutions down to 7 μm was tested. For this purpose, lipid distributions were visualized from transverse mouse kidney sections and Figure 4 displays the RGB MALDI-MS images (7 μm step size) of (A) [PS O-36:1+H]⁺ (red) [SM 34:1+H]⁺ (green) and [PE 38:0+K]⁺ (blue) in the positive and (B) [PA 36:1-H]⁻ (red), [HexCer 30:1-H]⁻ (green) and [SHexCer 42:2-H]⁻ (blue)

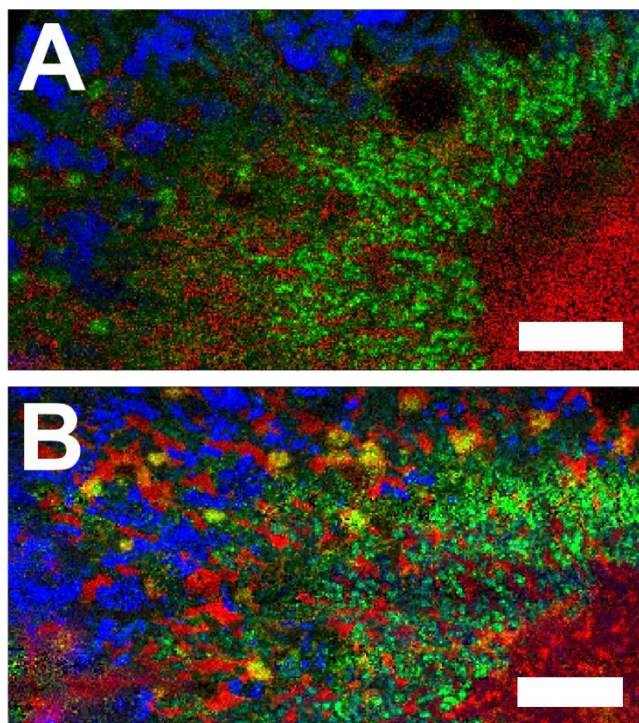


Figure 4. RGB MALDI-MS images of mouse kidney acquired in the (A) positive and (B) negative ion mode with 7 μm step size. The lateral resolved signal intensities of [PS O-36:1+H]⁺ (red, m/z 776.581), [SM 34:1+H]⁺ (green, m/z 703.575) and [PE 38:0+K]⁺ (blue, m/z 814.573) in the positive and [PA 36:1-H]⁻ (red, m/z 701.513), [HexCer 30:1-H]⁻ (green, m/z 642.485) and [SHexCer 42:2-H]⁻ (blue, m/z 888.623) in the negative ion mode were superimposed. The scale bars reflect 400 μm .

in the negative ion mode. Fluorescence microscopy images of post-MALDI-MSI immunofluorescence stained sections and fluorescence microscopy following Supporting Protocol 1 are shown in Figure S12. A comparison of MSI results in Figure 4 and microscopic images in Figure S12 allows us to correlate histological regions, e.g. glomeruli with synaptopodin, with mass spectrometrically recorded lipid distributions. Whereas [PS O-36:1+H]⁺ and [PA 36:1-H]⁻ are associated with the inner renal medulla and the renal tubules, [SM 34:1+H]⁺ and [HexCer 30:1-H]⁻ are located in the outer renal medullary interstitium regions and the glomeruli. High signal intensities of [PE 38:0+K]⁺ and [SHexCer 42:2-H]⁻ are associated with the renal cortex.⁴⁹ Further MS images are presented in Figure S13 and S15 for both ion polarities and 7 μm pixel size and 10 μm pixel size in Figure S16. For example, the regions with low or no ion intensity in Figure 4 are renal blood vessels (Figure S14) and are linked with other lipids such as [PC 34:0+H]⁺ (Figure S13G). In addition to unfunctionalized lipids, BzPy allows to image lipid+BzPy ion signals. Representative examples are shown in Figure S17 (positive ion mode) and Figure S18 (negative ion mode) and indicate that the lateral distribution of BzPy-derivatized lipids and unfunctionalized compounds is similar. For example, high signal intensities of [SM 34:1+H]⁺ (Figure S17A, left) and [SM 34:1+BzPy+H]⁺ (Figure S17A, right) are linked to the medullary interstitium and glomeruli. Additionally, the correlation between MALDI-MSI and optical microscopy suggests that no wash-out effects occur with BzPy as MALDI matrix and that BzPy can be used to visualize and

differentiate histological features in tissue with down to 7 μm in positive and negative ion mode.

On-tissue DB assignment of lipids. To investigate the capabilities of BzPy as reactive matrix for lipid DB position assignment in complex lipid mixtures, mouse cerebellum, kidney, and pancreas tissue was studied in positive and negative ion mode. Representative MALDI-MS² results for [SHexCer 42:2+BzPy-H]⁻ (mouse cerebellum), [PC 36:2+BzPy+H]⁺ (mouse pancreas) and [PC O-38:6+BzPy+H]⁺ (mouse kidney), [PC 36:4+BzPy+H]⁺ (mouse pancreas), [PC 36:3+BzPy+H]⁺ (mouse pancreas) and [PC 34:1+BzPy+H]⁺ (mouse pancreas) are shown in Figure 5 and S19 and S20B, respectively. For all compounds, α and/or ω ions enabled the assignment of DB positions. Whereas retro-PB fragments for SHexCer 42:2, PC O-38:6 and PC 36:4 are consistent with the presence of only a single DB position isomer, multiple isomers are present for PC 34:1 (Figure 20B), PC 36:2 (Figure 5B) and PC 36:3 (Figure S19C). In particular, α/ω ions for PC 34:1, PC 36:2 and PC 36:3 point to the presence of two, three and five DB positions, respectively. For example, retro-PB fragment ions of PC 36:2 indicate that mono- and diunsaturated FAs, e.g. PC 18:1_18:1 and PC 18:0_18:2, are combined and that their DBs are localized at $n-6$, $n-7$ and $n-9$. Fragment ions of PC 36:2 wherein all DBs are lost allow to connect them to either mono- or diunsaturated FAs. This is because corresponding neutral loss channels from a diunsaturated FA contain intact DBs, shifting the neutral loss by -2.016 Da (green box) compared to fragment ions stemming from monounsaturated FAs. DB retaining fragment ions alone does not allow to distinguish mono- and diunsaturated FAs but in combination with the lack of unsaturated neutral losses indicates the presence of a monounsaturated FA.

These results indicate that BzPy allows DB assignment of mono- and polyunsaturated lipids in positive and negative ion mode directly from tissue.

Resolving DB position isomers in pancreatic β -cells. To demonstrate the improvement in lateral resolution for DB position isomer localization when using BzPy compared to BPH, mouse pancreas tissue sections were investigated with MALDI-MS²I. An average overview MALDI mass spectrum is shown in Figure S20A revealing endogenous lipids and corresponding PB products detected in pancreas tissue. MALDI-MSI distributions of lipids were largely in line with previous studies of pancreas tissue.⁵⁰ Multiple BzPy-derivatized lipid ion signals were subjected to MALDI-MS²I. Namely, protonated signals of PC 34:1+BzPy, PC 36:2+BzPy, PC 36:4+BzPy, and PC 34:2+BzPy were fragmented and α_A ions were employed to visualize lateral DB position isomer distributions with 10 μm pixel size (Figure 5, S21 and S22). To the best of our knowledge, this is the highest reported lateral resolution for DB position isomer imaging. Protonated PC 34:2+BzPy and PC 36:4+BzPy did not show DB position isomerism and consequently all DB fragment ions show similar lateral distributions (Figure S22). In contrast, protonated PC 34:1+BzPy and PC 36:2+BzPy possess several isomers with DBs in the positions $n-9$ and $n-7$ and $n-9$, $n-7$, and $n-6$, respectively. The lateral distributions of these isomers differ. Local upregulation of mass spectrometric intensities linked with the $n-9$ isomer of PC 34:1 is observed in circular areas with 50 – 150 μm diameter (Figure 5C). In contrast, the intensity of $^7\alpha_A$ ions is decreased or even zero in the same regions (Figure 5D). Post-MALDI-MS²I immunofluorescence staining and subsequent fluorescence microscopy was performed to assign PC 34:1 isomer distributions to specific histological regions in

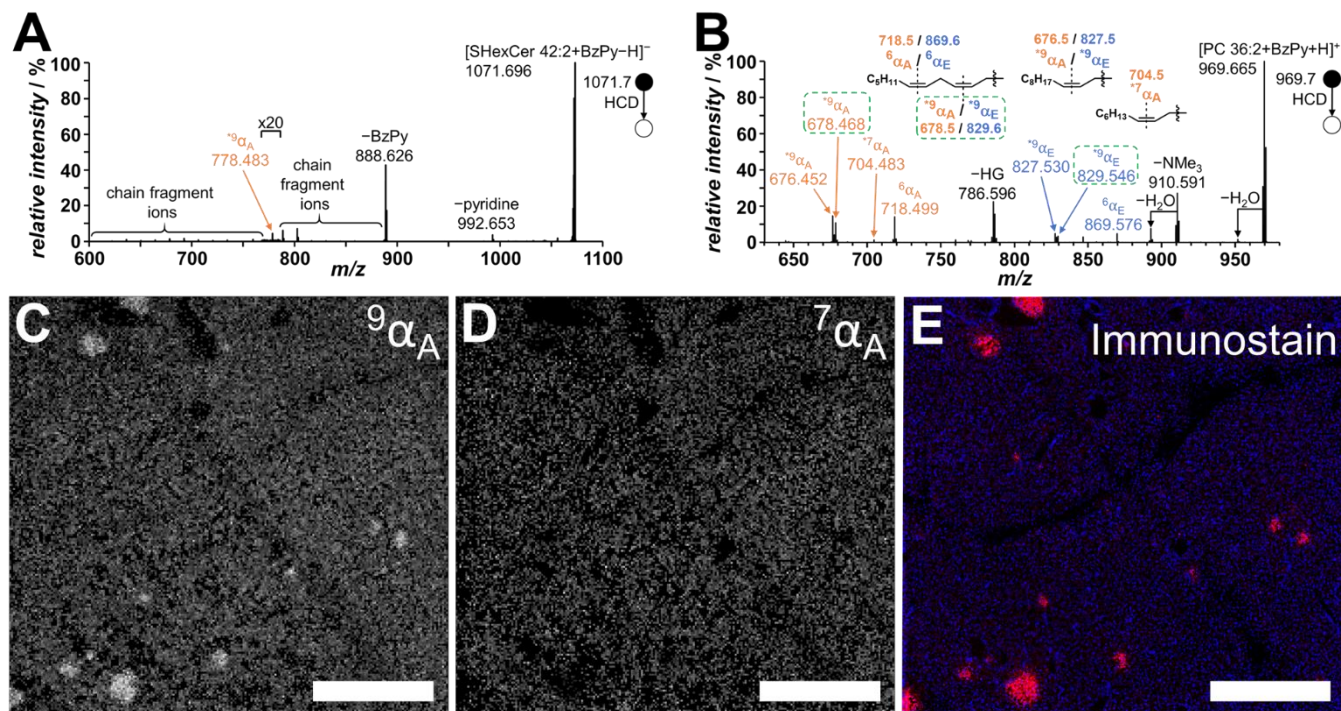


Figure 5. MALDI-MS² spectra of (A) [SHexCer 42:2+BzPy-H]⁻ and (B) [PC 36:2+BzPy+H]⁺ directly desorbed from mouse cerebellum and mouse pancreas tissue, respectively. In (B) * indicates DB position specific fragments. TIC normalized MALDI-MS² images of diagnostic fragment ions (C) ⁹α_A (*m/z* 650.439) and (D) ⁷α_A (*m/z* 678.470) of DB position isomers of [PC 34:1+BzPy+H]⁺ were acquired from mouse pancreas tissue with 10 μm pixel size. (E) Fluorescence microscopy image of the post-MALDI-MSI-immunofluorescence stained pancreas tissue section. Red areas in E indicate insulin-positive β-cells in Langerhans islets. The scale bars reflect 600 μm.

pancreatic tissue and results are shown in Figure 5E. Red fluorescence indicates the location of Langerhans islet, whereas cell nuclei are colored blue. A comparison to MALDI-MS²I results for PC 34:1 with fluorescence microscopy reveals that tissue regions with high ⁹α_A and low ⁷α_A intensities are correlated with the location of pancreatic islet. Differing lateral distributions were also observed for the DB position isomers of PC 36:2. The α_A ions of the PC 36:2 isomer possessing a diunsaturated FA with DBs in position *n*-6 and *n*-9 are homogeneously distributed (Figure S21A – S21B). In contrast, ⁹α_A and ⁷α_A ions of the isomers with two monounsaturated FAs are both enriched in the pancreatic islets (Figure S21C – S21D). In mice Langerhans islets predominantly consist of β-cells.⁵¹ Consequently, the increased mass spectrometric abundances in pancreatic islets is directly linked to β-cells and is distinctly different from the surrounding tissue. This finding suggests that the enriched lipid DB position isomers fulfill specific functions in β-cells or are linked to metabolic reactions in β-cells that predominantly give rise to the imaged lipids.

CONCLUSIONS

Screening of twelve PB reactive aromatic carbonyl compounds revealed pyridine derivatives of BPh as novel PB reactive MALDI matrices for DB position resolved MALDI-MS²I and high-resolution dual polarity MALDI-MSI studies. In particular, BzPy improves ion intensities, PB yield, and number as well as relative signal intensities of DB position diagnostic fragment ions compared to BPh. *In situ* PB functionalization using PB reactive MALDI and DB localization is presented for GPLs, SLs, and a TG in the positive ion mode as well as for a FA and a SHexCer in the negative ion mode. This extends the number

of lipid classes with addressable DB positions compared to previously reported desorption-based MS² strategies. PB and non-specific functionalization of lipids with BzPy during MALDI allows to increase lipid ion intensities and lipid coverage compared to BPh results. Namely, a total of 508/365 features were assigned in positive/negative ion mode including GPLs, GLs, SLs, STs, and FAs.

The capabilities of spatially-resolved lipidomics have been demonstrated by on-tissue MALDI-MS², MALDI-MSI, and MALDI-MS²I from different mouse tissues. On-tissue MALDI-MS² deciphered DB positions of multiple mono- and polyunsaturated PCs, including PC O-38:6. High-resolution dual polarity MALDI-MSI (7 μm) of mouse kidney allows us to link lateral distributions of endogenous lipids and histological features, such as glomeruli, by post-MSI immunofluorescence microscopy. In comparison to BPh (15 μm pixel size), the improvement in lateral resolution and detectable diagnostic fragment ions of MALDI-MS²I is showcased by DB position isomer resolved MS² images of PCs with down to 10 μm in mouse pancreas tissue sections. We observed up- and downregulation of the *n*-9 and *n*-7 isomers in areas that match with islets of Langerhans.

The caveat of our methodology, similar to other DESI and MALDI workflows, is the ion suppression effect that makes MALDI-MS²I experiments of low abundant lipids challenging. Even though the matrix BzPy has considerably increased lipid coverage, allowed negative ion mode investigations, and improved the lateral resolution compared to BPh, other wavelengths, matrix systems, or post-ionization schemes are most likely necessary to probe DB position isomerism for all lipid classes. These investigations are currently underway.

In terms of applications, we envision that the herein introduced BzPy matrix can be used to study local lipid isomer variations in pancreas and kidney tissue in the context of diabetes. Diabetes and related metabolic malfunctions have been linked with lipid, especially, local PC alterations in these organs and we are keen to explore spatially-resolved lipid isomerism to contribute to an understanding of altered lipid metabolism.

ASSOCIATED CONTENT

Supporting Information

A detailed description of experimental methods and protocols; MSI results using BzPy as MALDI matrix; solid-phase UV spectrum of BzPy; MALDI-MS² for various PB reactive matrices and lipid standards; additional tables and figures of assigned lipid classes; immunofluorescence results of mouse kidney; additional positive and negative ion mode MALDI-MSI results for kidney with 7 and 10 μm pixel size; comparison of endogenous and corresponding BzPy distributions in the kidney; additional DB-position resolved MALDI-MS² results for mouse kidney and pancreas sections; additional DB-position resolved MALDI-MS²I results for mouse pancreas sections.

AUTHOR INFORMATION

Corresponding Author

* E-mail: Sven.Heiles@anorg.chemie.uni-giessen.de (S.H.)

ORCID

Sven Heiles: 0000-0003-3779-8071

Author Contributions

S.H. supervised the project. S.H. and F.W. designed and F.W. performed the MS experiments. A.W. and F.M. designed and performed the immunofluorescence experiments. S.H. and F.W. discussed the findings and wrote the manuscript consulting A.W. for the immunofluorescence results.

Notes

The authors declare no competing financial interest.

ACKNOWLEDGMENT

S.H. thanks the Fonds der chemischen Industrie for financial support through a Liebig fellowship. Financial support by the Deutsche Forschungsgemeinschaft (HE 8521/1-1) and institutional funds (A.W.) is gratefully acknowledged. All authors thank Dr. Daniela Fietz (Institute of Veterinary Anatomy, Histology and Embryology, JLU Giessen) for providing mouse brain samples.

REFERENCES

- (1) Han, X. *Nat. Rev. Endocrinol.* 2016, 12, 668–679.
- (2) Yang, K.; Han, X. *Trends Biochem. Sci.* 2016, 41, 954–969.
- (3) Tsugawa, H.; Ikeda, K.; Takahashi, M., et al. *Nat. Biotechnol.* 2020, 1–5.
- (4) Harayama, T.; Riezman, H. *Nat. Rev. Mol. Cell Biol.* 2018, 19, 281–296.
- (5) Vriens, K.; Christen, S.; Parik, S., et al. *Nature* 2019, 566, 403–406.
- (6) Volmer, R.; van der Ploeg, K.; Ron, D. *Proc. Natl. Acad. Sci. USA* 2013, 110, 4628–4633.
- (7) Cunha, D. A.; Hekerman, P.; Ladrière, L., et al. *J. Cell Sci.* 2008, 121, 2308–2318.
- (8) Fu, S.; Yang, L.; Li, P., et al. *Nature* 2011, 473, 528–531.
- (9) Sustarsic, E. G.; Ma, T.; Lynes, M. D., et al. *Cell Metab.* 2018, 28, 159–174.e11.
- (10) Bergholt, M. S.; Serio, A.; McKenzie, J. S., et al. *ACS Central Science* 2018, 4, 39–51.
- (11) Ellis, S. R.; Paine, M. R. L.; Eijkel, G. B., et al. *Nat. Methods* 2018, 15, 515–518.
- (12) Murphy, R. C. *Tandem mass spectrometry of lipids*; Royal Society of Chemistry: Cambridge, 2015.
- (13) Vasilopoulou, C. G.; Sulek, K.; Brunner, A.-D., et al. *Nat. Commun.* 2020, 11, 331.
- (14) Feider, C. L.; Macias, L. A.; Brodbelt, J. S.; Eberlin, L. S. *Anal. Chem.* 2020, 92, 8386–8395.
- (15) Blevins, M. S.; James, V. K.; Herrera, C. M.; Purcell, A. B.; Trent, M. S.; Jennifer S. Brodbelt. *Anal. Chem.* 2020, 92, 9146–9155.
- (16) Klein, D. R.; Feider, C. L.; Garza, K. Y.; Lin, J. Q.; Eberlin, L. S.; Jennifer S. Brodbelt. *Anal. Chem.* 2018, 90, 10100–10104.
- (17) Fang, M.; Rustam, Y.; Palmieri, M.; Sieber, O. M.; Reid, G. E. *Anal. Bioanal. Chem.* 2020, 412, 2339–2351.
- (18) Narreddula, V. R.; Boase, N. R.; Ailuri, R., et al. *Anal. Chem.* 2019, 91, 9901–9909.
- (19) Pham, H. T.; Julian, R. R. *Int. J. Mass Spectrom.* 2014, 370, 58–65.
- (20) Paine, M. R. L.; Poed, B. L. J.; Eijkel, G. B., et al. *Angew. Chem. Int. Ed.* 2018, 57, 10530–10534.
- (21) Kirschbaum, C.; Saied, E. M.; Greis, K., et al. *Angew. Chem. Int. Ed.* 2020.
- (22) Feng, Y.; Chen, B.; Yu, Q.; Li, L. *Anal. Chem.* 2019, 91, 1791–1795.
- (23) Kuo, T.-H.; Chung, H.-H.; Chang, H.-Y., et al. *Anal. Chem.* 2019, 91, 11905–11915.
- (24) Esch, P.; Heiles, S. *Analyst* 2020, 145, 2256–2266.
- (25) Birk, F.; Fraatz, M. A.; Esch, P.; Heiles, S.; Pelzer, R., Holger Zorn. *J. Agric. Food Chem.* 2019, 67, 13460–13469.
- (26) Cao, W.; Cheng, S.; Yang, J., et al. *Nat. Commun.* 2020, 11, 375.
- (27) Li, H.-F.; Cao, W.; Ma, X.; Xie, X.; Xia, Y., Zheng Ouyang. *J. Am. Chem. Soc.* 2020, 142, 3499–3505.
- (28) Esch, P.; Heiles, S. *J. Am. Soc. Mass Spectrom.* 2018, 29, 1971–1980.
- (29) Ma, X.; Xia, Y. *Angew. Chem. Int. Ed.* 2014, 53, 2592–2596.
- (30) Jeck, V.; Froning, M.; Tiso, T.; Blank, L. M.; Hayen, H. *Anal. Bioanal. Chem.* 2020, 1–13.
- (31) Xie, X.; Zhao, J.; Lin, M.; Zhang, J.-L.; Xia, Y. *Anal. Chem.* 2020, 92, 8487–8496.
- (32) Spraggins, J. M.; Djambazova, K. V.; Rivera, E. S., et al. *Anal. Chem.* 2019, 91, 14552–14560.
- (33) Bednařík, A.; Bölsker, S.; Soltwisch, J.; Dreisewerd, K. *Angew. Chem. Int. Ed.* 2018, 57, 12092–12096.
- (34) Bednařík, A.; Preisler, J.; Bezdeková, D., et al. *Anal. Chem.* 2020, 92, 6245–6250.
- (35) Wäldchen, F.; Spengler, B.; Heiles, S. *J. Am. Chem. Soc.* 2019, 141, 11816–11820.
- (36) Porta Siegel, T.; Ekroos, K.; Ellis, S. R. *Angew. Chem. Int. Ed.* 2019, 58, 6492–6501.
- (37) Heiles, S.; Kompauer, M.; Müller, M. A.; Spengler, B. *J. Am. Soc. Mass Spectrom.* 2020, 31, 326–335.
- (38) Gilmore, I. S.; Heiles, S.; Pieterse, C. L. *Annu. Rev. Anal. Chem.* 2019, 12, 201–224.
- (39) Kampmeier, J.; Dreisewerd, K.; Schürenberg, M.; Strupat, K. *Int. J. Mass Spectrom.* 1997, 169–170, 31–41.
- (40) Cerruti, C. D.; Benabdellah, F.; Laprévotte, O.; Touboul, D.; Brunelle, A. *Anal. Chem.* 2012, 84, 2164–2171.
- (41) Huang, P.; Huang, C.-Y.; Lin, T.-C., et al. *Anal. Chem.* 2020, 92, 7139–7145.
- (42) Calvano, C. D.; Monopoli, A.; Cataldi, T. R. I.; Palmisano, F. *Anal. Bioanal. Chem.* 2018, 410, 4015–4038.
- (43) Liebisch, G.; Vizcaíno, J. A.; Köfeler, H., et al. *J. Lipid Res.* 2013, 54, 1523–1530.
- (44) Hankin, J. A.; Barkley, R. M.; Murphy, R. C. *J. Am. Soc. Mass Spectrom.* 2007, 18, 1646–1652.
- (45) Paschke, C.; Leisner, A.; Hester, A., et al. *J. Am. Soc. Mass Spectrom.* 2013, 24, 1296–1306.
- (46) Lin, Q.; Zhang, D.; Xia, Y. *Analyst* 2020, 145, 513–522.
- (47) Boskamp, M. S.; Soltwisch, J. *Anal. Chem.* 2020, 92, 5222–5230.

(48) Kettling, H.; Vens-Cappell, S.; Soltwisch, J., et al. *Anal. Chem.* 2014, 86, 7798–7805.

(49) Bowman, A. P.; Bogie, J. F. J.; Hendriks, J. J. A., et al. *Anal. Bioanal. Chem.* 2020, 412, 2277–2289.

(50) Prentice, B. M.; Hart, N. J.; Phillips, N., et al. *Diabetologia* 2019, 62, 1036–1047.

(51) Nie, J.; Liu, X.; Lilley, B. N., et al. *Proc. Natl. Acad. Sci. USA* 2013, 110, 13857–13862.